Effects of bond gap thickness on the fracture of nano-toughened epoxy adhesive joints

V. Cooper[a], A. Ivankovic[a,*], A. Karac[b], D. McAuliffe[a] and N. Murphy[a]

[a] *School of Mechanical and Materials Engineering, University College Dublin, Ireland*

[b] *Faculty of Mechanical Engineering, University of Zenica, Bosnia and Herzegovina*

Abstract

The current work is a combined experimental-numerical study of the fracture behaviour of a nano-toughened, structural epoxy adhesive. The mode I fracture toughness of the adhesive is measured using tapered double-cantilever beam (TDCB) tests with various bond gap thicknesses ranging from 0.25mm - 2.5mm. Circumferentially deep-notched tensile specimens are independently employed to measure the cohesive strength of the adhesive as a function of constraint. The experimental TDCB test results are predicted numerically for each bond gap thickness using the Finite Volume method and a Dugdale cohesive zone model. A unique relationship between the fracture energy and the constraint level is established. The effect of bond gap thickness on the fracture behaviour of TDCB joints is hence directly attributed to the variation of the intrinsic fracture energy with constraint and not to the variation of the 'far field' plastic zone size with bond gap thickness. Using the well known Rice and Tracey void growth model, a link is established between the voids observed in the fracture process zone, the constraint imposed by the thickness of the adhesive and the resulting fracture energy.

Keywords: Adhesion and adhesives; Fracture toughness; Crack tip plasticity; Voids and inclusions; Elastic-plastic material.

* Corresponding author. Tel.: +353 1 7161994; fax. +353 1 2830534.
E-mail address: alojz.ivankovic@ucd.ie (A. Ivankovic).

1.0 Introduction

The accurate and efficient determination of the fracture toughness and the associated fracture mechanisms of a structural adhesive are of fundamental importance to adhesive manufacturers and end users alike. The ability to predict the behaviour of such joints can lead to better designs, increased performance, reduced costs and enhanced safety. Better understanding of the structure-property relationship will ultimately lead towards improved adhesives with tailored properties. However, the behaviour of joints in real structures is difficult to predict since their behaviour, including the failure mechanisms, are complex to measure and model. The testing of prototypes and trial structures is costly and time-consuming. Consequently, there has been a growing motivation for the development of theoretical models for predicting the damage and failure of adhesive joints. These models require geometry independent material parameters, which are usually obtained from tests with simpler geometries and subsequently applied in the analysis of more complex geometries.

An important parameter in adhesive joint design is the bond gap thickness (BGT) which needs to be accurately controlled in order to obtain a consistent and reliable joint strength. However, no simple relationship between fracture energy and BGT exists. Many studies have been carried out to investigate the effect of bond thickness on the fracture behaviour of adhesive joints [1–5]. It appears from most of these investigations that the critical fracture energy of adhesive joints reaches a maximum value G_{ICm} at some bond gap thickness h_m. Mostovoy et al. [5] investigated the effects of adhesive joint geometry on the toughness of commercial toughened epoxy adhesives with aluminium adherends and found that an increase in bond gap thickness resulted in an increase in toughness. Bascom et al. [1] also investigated the behaviour of rubber-modified epoxy resin using the tapered double-cantilever beam (TDCB) configuration and found that the fracture energy is maximized when the bond thickness equals the diameter of the plastic zone formed ahead of the crack tip. Kinloch and Shaw [3] explained that the adhesive fracture energy G_{IC} depends on the size of the plastic zone, and that the constraining effects from the two adherends control the plastic zone size. When the bond thickness is less than h_m, the plastic zone cannot fully develop due to the restriction imposed by the substrates. When the bond thickness becomes larger than h_m, the plastic zone is no longer constrained by the substrates and hence fracture energy should plateau. The maximum, G_{ICm}, is reached when the adhesive

layer thickness and the plastic zone diameter $2r_y$ are approximately equal. Thus, it was shown that the adhesive thickness, h_m at G_{ICm} should be expressed by:

$$h_m = 2r_y = \frac{1}{\pi}\frac{EG_{IC(bulk)}}{\sigma_y^2} \quad (1)$$

where r_y is Irwin's first order estimate of the plastic zone size under plane stress conditions, E is the adhesive modulus, $G_{IC(\text{bulk})}$ is the mode I fracture energy of the bulk adhesive specimen and σ_y is the uniaxial yield strength of the adhesive [6].

Lee et al. [2] investigated the bond gap thickness effect on fracture toughness and pointed out that the presence of toughening agents (rubber particles) in the adhesive might have caused changes in the crack propagation direction as the bond gap thickness changes. Recently, Kawashita et al. [7] presented peel test data from aluminium joints with bond gap thicknesses of 0.1 mm, 0.25 mm and 0.4 mm, for two rubber toughened epoxy adhesives. The measured fracture toughness values increased with bond gap thickness and a reasonable fit was obtained between the test results and their LEFM model. The thickness and width of the adhesive layer affects the stress and strain distribution in the adhesive. For example, a change of the adhesive layer thickness can cause a transition from small-scale yielding conditions within the adhesive to fully plastic conditions [8]. Azari et al. [9] used aluminium DCB joints and reported a linear increase of mode I fracture energy of a toughened epoxy adhesive with BGT which was varied between 0.13 and 0.79 mm. They attributed this variation to the finite element (FE) predicted linear variation of the plastic zone area with BGT [10]. In addition, they estimated the value of constraint factor along the crack front for two adhesives. It was found that the constraint factor in the middle of the specimen for an adhesive with fracture energy of 200 J/m^2 varied from 2.2 for 0.79 mm BGT to 2.7 for 0.13 mm BGT, while for an adhesive with G_{IC} = 400 J/m^2, the constraint factor varied from 2.4 to 2.8 as the BGT changed from 0.79 to 0.13 mm.

In the current work, the mode I fracture behaviour of a nano-toughened, structural epoxy adhesive was examined using low-rate TDCB tests with various bond gap thicknesses. The variation of the adhesive fracture energy, G_{IC}, with bond gap thickness was addressed by quantifying the level of constraint within the bond line which was estimated numerically as a function of BGT. Numerical modelling of the experiments was performed using the finite volume method and Dugdale shape cohesive zone model (CZM). In parallel to this work, circumferentially deep-notched tensile (CDNT) specimens were employed in an attempt to

directly characterise the traction-separation laws of the adhesive. A detailed analysis of the fracture surfaces, using scanning electron microscopy, revealed variations of the micro-structural features with BGT and hence constraint. The void diameters on the TDCB fracture surfaces were measured and the fracture strain was estimated for different bond gap thicknesses. The fracture strain was found to vary with BGT in a similar fashion to the G_{IC} variation with BGT. The results were found to follow the Rice and Tracey void growth model [11] as a function of constraint. The measured void growth and Rice and Tracey model were then successfully employed to explain quantitatively the source of dependency of G_{IC} with constraint.

2.0 Application of the CZM to adhesive joints

Cohesive zone models are widely used to model the fracture of adhesive joints. In general, the substrates are modelled as elastic-plastic continua while two main approaches are adopted for the modelling of the adhesive layer: *i)* CZM is used to represent the entire adhesive layer, *ii)* the adhesive layer is modelled as a continuum while CZM is used to describe the local fracture process. A number of authors have used a single row of cohesive zone elements to represent the adhesive layer, e.g. [12–15]. However, the use of a single cohesive zone to describe the entire response of an adhesive layer is an over simplification since the fracture of an adhesive layer may be very complex, involving bulk plastic deformation of the adhesive, various types of damage phenomena developing at different scales, crack deflection, multiple cracking etc. [8]. Also, the cohesive law used in such models has to be a function of the adhesive layer thickness [12]. More advanced models consider both the continuum behaviour and fracture process of the adhesive layer, e.g. [8,16–19]. Such models contain a finite thickness adhesive layer usually represented by an elastic-plastic material model, in which a row of cohesive zone elements is embedded representing the fracture process within the adhesive.

Li et al. [20] experimentally determined the mode I and mode II cohesive parameters and used a cohesive zone approach to model the mixed mode fracture of adhesive joints. Ferracin et al. [19] carried out a numerical study to analyse the mode I steady-state debonding in a wedge-peel test and proposed procedures for identifying the cohesive zone parameters from wedge-peel measurements. Pirondi [21] simulated the fracture of a pre-cracked DCB joint bonded with a commercial adhesive using a cohesive zone model and investigated the influence of the cohesive zone parameters (shape, σ_{max}) on the force-

displacement results. The results showed good agreement with experiments with respect to the stiffness and the peak load but overestimated the crack propagation load. The cohesive parameters for both tough and brittle modes of crack growth were determined in the work of Sun et al. [22,23] by comparing numerical predictions from cohesive zone simulations to the experimental results obtained using DCB specimens and tensile tests. Li et al. [24] used a cohesive-zone approach to model the mode I fracture of adhesively bonded composite joints. They used a triangular type traction-separation law to predict the strengths and deformation of the joints and also the transition between composite and interfacial failures. Previous studies have indicated that a Dugdale shape CZ law can also be used to accurately predict the fracture behaviour of adhesively bonded joints [25–27].

Pardoen et al. [8] employed a quasi-static steady-state FE method to model the wedge-peel test, and investigated the variation of adhesive fracture energy as a function of specimen geometry. The adherends were modelled as a strain hardening elastic-plastic material. It was proposed that the adhesive fracture energy G_{Ic} can be partitioned into G_0 the intrinsic work of fracture represented by the cohesive zone response and G_P the contribution arising from the far-field plastic energy dissipation and stored elastic energy within the adhesive layer. Therefore the adhesive fracture energy was evaluated as:

$$G_{Ic} = G_0 + G_p \tag{2}$$

The results obtained in [8] showed a dependence of G_{Ic} upon both the adhesive layer and adherent thicknesses. The authors explained this dependency in terms of constraint effects on G_P, while G_0 was assumed to be independent of constraint and BGT. A similar energy partitioning approach was reported in [28], where a steady-state FE model was used to study energy contributions in peel tests. It was found that the values of G_{Ic} were not significantly dependent upon the details of the peel test configuration and that numerical predictions agreed well with reported analytical results from various elastic-plastic peel tests. This was attributed to the fact that the main contribution to G_{Ic} arose from the intrinsic work of fracture, i.e. the energy dissipated locally ahead of the crack tip, while the far-field plasticity occurring in the adhesive (but outside the fracture process zone), had a secondary effect.

2.1 Constraint dependent CZM

The stress and strain fields at the tip of a crack in an adhesive are significantly influenced by the level of constraint (or stress triaxiality) imposed by the surrounding adherends and the adhesive joint geometry. An important prerequisite for the application of cohesive zone models is the determination of its parameters over a wide range of stress states [29]. In the CZM approach, it is generally accepted that the two parameters which have the most pronounced effect on the prediction of the fracture process are G_{IC} and the cohesive strength σ_{max} where σ_{max} is assumed to be the critical, limiting maximum value of the stress in the damage zone ahead of the crack. The actual shape of the CZM is usually found to have secondary influence on the material separation behaviour [30]. This is particularly the case for problems with single, slowly propagating cracks. For rapid crack propagation in brittle materials the shape of the CZM has been found to play a much stronger role [31]. A number of studies on ductile failure due to void growth strongly indicate that these two parameters are stress state dependent, e.g. [29,32–34]. In fracture mechanics the stress triaxiality, i.e. the ratio of hydrostatic to equivalent stress, is most commonly used to quantify the local crack tip constraint [35]. Siegmund [36] and later Scheider [37] used FE simulations to predict the deformation behaviour of ductile metals using a single-void unit cell. They demonstrated that, due to the micromechanisms of void growth and coalescence, the energy dissipation rate is not a material constant. Instead, this quantity was found to depend on the specimen geometry and size as well as on the amount of crack extension. They proposed a cohesive zone model in which the traction-separation law is triaxiality dependent. In another numerical study, Siegmund and Brocks [35] demonstrated that the parameters of the cohesive zone in ductile materials were influenced by the triaxiality of the stress state. Ting et al. [38,39] conducted an extensive experimental study on ductile polymers and directly measured CZM parameters as a function of rate and constraint using CDNT type geometry. σ_{max} was found to increase with increasing constraint whereas the critical separation δ_c was found to decrease with increasing constraint. The evidence suggests that the cohesive process is neither independent from the global constraint nor from that experienced locally throughout the crack growth history. Higher triaxiality normally causes an increase in the maximum stress and a decrease in ductility.

3.0 Materials

3.1 Substrates

A requirement of the TDCB test is that the substrates should remain within the elastic region throughout the test. For this reason, a high yield strength substrate material must be used. In the current work, aluminium Al2014-T6 and steel EN24T are selected. The mechanical properties of both materials are given in Table 1 where E is the Young's modulus, σ_y the 0.2% proof yield stress, UTS the ultimate tensile strength, ρ the mass density and ν the Poisson ratio. The substrate surfaces were pre-treated in order to enhance bonding between the substrate and adhesive and obtain cohesive fracture in the adhesive. The surface treatment for the aluminium consisted of an acetone degrease followed by a grit blast (180/220 mesh grit). After the grit blast, the beams were rinsed in hot water, dried, and wiped once more with acetone. The beams were then placed in a chromic acid etch bath which was pre-heated to 60 - 65°C for 30 minutes [40]. After the etching, the substrates were removed from the bath and immersed in a tank of running water at ambient temperature for a further 15 minutes. The pre-treated specimens were then placed in an air-circulating oven at 50°C, allowed to dry for 30 minutes and bonded immediately to avoid contamination of the pre-treated surfaces. A similar surface preparation was carried out on the steel substrates but, in this case, the acid etching was not required.

Table 1. Mechanical properties of the substrate materials.

Material	$\boldsymbol{E}$ [GPa]	σ_y [MPa]	***UTS*** [MPa]	ρ [kg/m^3]	ν [–]
Al 2014-T6	72.4	425	472	2800	0.33
Steel EN24T	205	875	1000	7850	0.29

3.2 Adhesive

Henkel Lab ref. 3019-98 is an experimental grade of a rubber-toughened, hot-cured structural epoxy adhesive which is supplied in the form of one-component paste. This adhesive contains essentially 3 toughening agents - two core shell particle grades and one liquid elastomer co-toughener. Core-shell particles generally have a core consisting of a polymeric material having elastomeric or rubbery properties. This is surrounded by a shell comprised of a non-elastomeric polymeric material, i.e. a thermoplastic or thermoset/crosslinked polymer. The first grade of core-shell rubber particles with approximately 50 nm diameter is supplied as a pre-dispersion in an epoxy resin giving an overall volume fraction for 50 nm particles of 13%. The second core-shell particle grade is

also a nano-sized core-shell rubber with approximately 200 nm diameter and is mixed as a powder with 48% overall volume fraction. The formulation also contains Epon 828 resin (13% by volume). This is a commercially available epoxy resin which is widely used in formulation and fusion technology.

Tensile tests were carried out on bulk adhesive specimens to obtain the mechanical properties at low loading rate (0.1 mm/min). The geometry was manufactured to the dimensions of type '5A' designated in the standard ISO 527-2 i.e. 75 mm long, 30 mm gauge length [41]. The yield stress σ_y was calculated based on the 0.2% proof stress. A typical stress-strain curve of the adhesive is shown in Fig. 1 and the mechanical properties are summarised in Table 2.

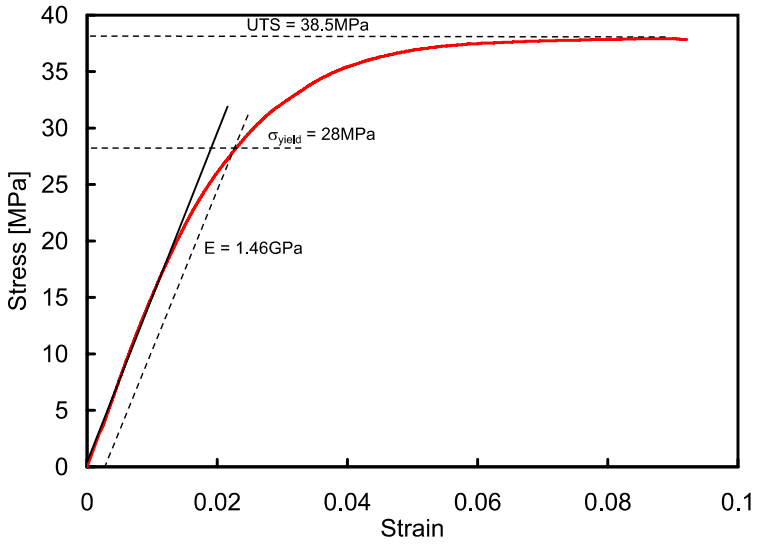

Fig. 1. Stress-strain curve for Henkel 3019-98 adhesive at 0.1 mm/min (strain rate = 6.66 10^{-5} s^{-1}).

Table 2. The mechanical properties of the adhesive.

E [GPa]	σ_y [MPa]	UTS [MPa]	ρ [kg/m^3]	ν [–]
1.46	28	38.5	1300	0.4

4.0 Experimental work

4.1 The tapered-double cantilever beam test

The mode I fracture of the adhesive joints was examined using the TDCB specimen. Two TDCB configurations were used according to: *(i)* ASTM protocol with steel substrates of 25.4 mm width [42] and *(ii)* BS protocol with 10 mm wide aluminium substrates [43]. Schematics of both TDCB geometries are shown in Fig. 2. Tests were conducted at low loading rates and

at room temperature on joints with various bond gap thicknesses ranging from 0.25 mm to 2.5 mm. In order to achieve a linear change of compliance with the crack length, the height of the specimen is varied by contouring the substrate beam so that:

$$m = \frac{3a^2}{h_a^3} + \frac{1}{h_a} = \text{constant}, \tag{3}$$

where m is referred to as the geometry factor and h_a is the thickness of the substrate beam (adherent) at a crack length a. The corrected beam theory (CBT) method of analysis is used to deduce G_{IC} from the TDCB test (Blackman et al., 2003).

$$G_{IC}(CBT) = \frac{4P^2}{EB^2} m \left[1 + 0.43 \left(\frac{3}{ma} \right)^{\frac{1}{3}} \right], \tag{4}$$

where P is the load at crack length a and B is the specimen width.

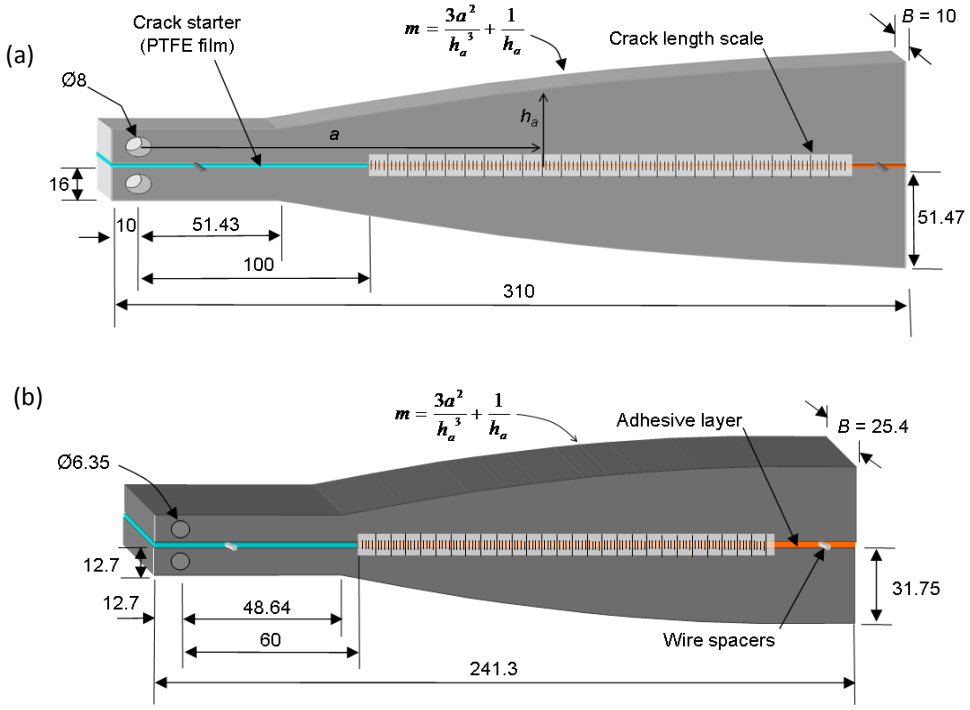

Fig. 2. Illustration of the TDCB geometries according to (a) British Standard BS 7991 (2001) (m = 2 mm^{-1}) and (b) ASTM D 3433 (1999) (m = 3.543 mm^{-1}). All dimensions in millimetres.

The BGT was controlled by placing a stainless steel wire spacer at either end of the substrates. As specified in the test protocols, a 12.5 μm thick, non-stick polytetrafluoroethylene (PTFE) film, was inserted at one end to act as a crack starter in the adhesive layer. The length of the film varied depending on the geometry to be manufactured; 100 mm from the load-line for the 10 mm wide aluminium specimens and 60 mm from the load-line for the 25.4 mm wide steel geometry. The specimens were placed in a specially designed bonding jig that maintained alignment and applied a slight compressive load during cure. The excess adhesive was removed from the side of the beams prior to curing. The adhesive was cured at 180°C for 30 minutes. A thermocouple lead was inserted in to the bond-line to monitor the temperature during cure.

After the curing cycle, a thin layer of correction fluid (i.e. Tipp-ex) was painted along the adhesive on one side of the joint. A grid with 5 mm spacing was then drawn on the white background using a thin marker to enable crack length measurements to be taken during the test. The tests were carried out at a constant test rate using a screw driven tensile testing machine (Hounsfield H50KS) equipped with a 10 kN load cell. The crosshead speed for the narrow geometry was set to 0.5 mm/min and to 0.3 mm/min for the wide geometry. The crack length measurements were recorded at 5 mm increments using a travelling microscope. All tests were performed under controlled conditions of approximately 50% relative humidity (RH) and a temperature of 23 ± 1°C.

4.2 The circumferentially deep notch tensile test

There is a lack of experimental methods for the direct measurement of traction-separation (TS) curves. This is mainly due to difficulties in: i) obtaining conditions in the specimen representative of those at the crack, and ii) achieving uniform damage distribution and separation across a section of the specimen thus avoiding crack growth. The CDNT test was previously used for the direct measurement of traction-separation curves in tough polymers such as polyethylene under different rate and constraint conditions [38,39,45–47]. This test was also found to be successful in classifying various grades of polymers in terms of their fracture performance.

In the present work, the CDNT test is adopted and further developed for use with adhesives. The main idea as well as the challenge of the test is that the damage and separation processes of the adhesive develop uniformly across, and are confined within, a constrained region of a notched ligament. Varying the notch depth results in a corresponding change in

the level of constraint within the ligament which would mimic the constraint imposed on the process region ahead of a crack tip in an adhesive joint. The localised deformation and damage processes in the notched ligament should be representative of those present at a crack tip and allow a measurement of these processes, independent of the bulk deformation of the specimen.

Bulk cylindrical adhesive specimens, 10 mm in diameter and 85 mm long, were cast using a specially designed PTFE-coated mould. A circumferential notch was introduced in the centre of each sample. The notch was machined on a lathe using a single point cutting tool. The notch depth was varied to give three different ligament to bulk area (LBA) ratios: 25%, 35%, and 50%. The geometry of the notch, i.e. the depth and the tip radius, should be such that crack initiation is prevented while uniform damage and separation is preserved within the ligament. The notch geometry that gave the most reliable results consisted of a 55° included angle with a 0.4 mm tip radius. Details of the effects of other notch geometry types are outlined in [48]. The test specimen was mounted on a tensile test machine using precision custom made stainless steel fittings as shown in Fig. 3. The load was recorded by the load cell and the displacement by a clip-gauge extensometer over 8 mm gauge length. For a given displacement, the traction was obtained by dividing the load by the original ligament area, giving the traction-displacement curve for a given constraint. All tests were carried out under quasi-static conditions at 0.05 mm/min and room temperature.

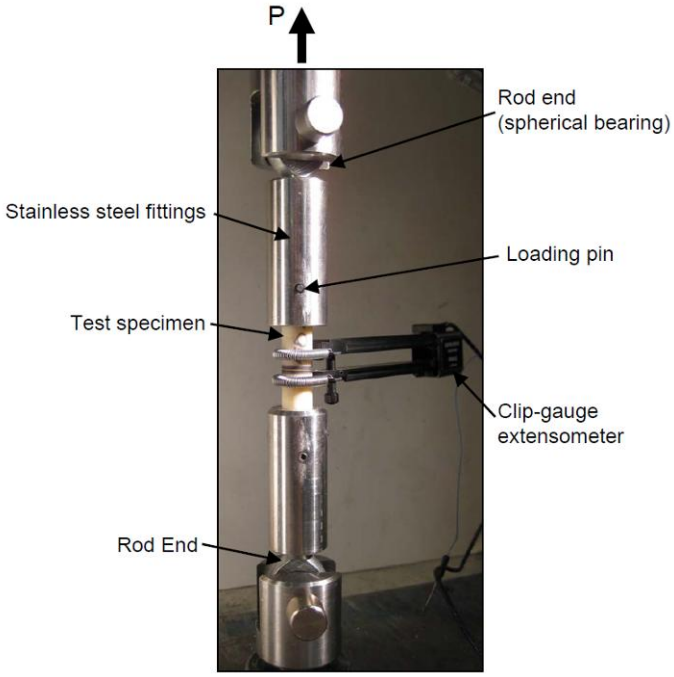

Fig. 3. Bulk CDNT test experimental setup.

5.0 Experimental Results

5.1 TDCB results

A series of TDCB tests with bond gap thicknesses ranging from 0.25 mm to 2.5 mm were carried out using the two different TDCB geometries described earlier. In both configurations, a mode I cohesive fracture was observed in each test where the BGT was less than approximately 1 mm (Fig. 4a). When the BGT was increased above 1 mm, a significant change in the crack behaviour was observed. Shear lips were formed on the stress-free sides of the specimen and a local mode III loading was introduced forcing the fracture to change from plane cohesive mode I to slant mixed-mode I and III fracture. After initiating as a predominantly mode I crack, a through-thickness fracture profile with a component of mode III loading gradually developed across the specimen resulting in a flat triangular region in front of the initial pre-crack followed by the slant fracture (Fig. 4b).

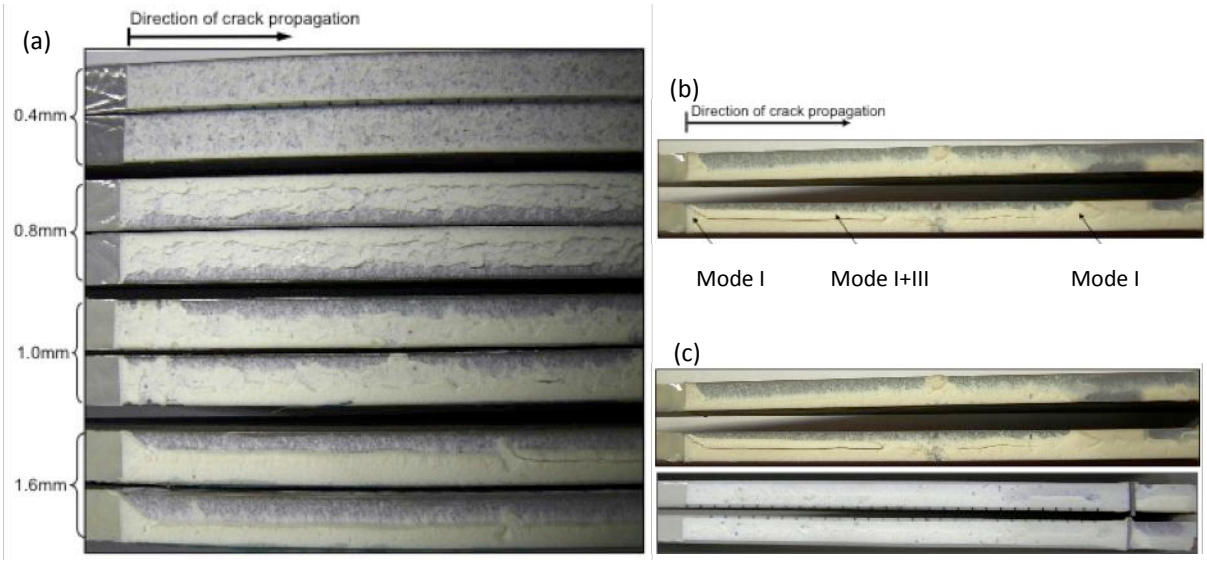

Fig. 4. (a) Typical fracture surfaces of 10 mm wide Aluminium TDCB specimens with various BGT, (b) features on a 2 mm BGT fracture surface, (c) top; no side groove, bottom; side groove.

In order to produce a flat, mode I cohesive fracture for the entire range of bond gap thicknesses, side grooves were machined in the adhesive layer to a depth of 1 mm using a 45^{o} double-angle cutting tool. The main purpose of the side grooves was to eliminate the free surfaces on the fracture plane and hence reduce plasticity, shear lips and slant fracture (Fig. 4c). They also acted to create a weak crack plane to guide the direction of the crack through the adhesive and to ensure symmetrical mode I plane strain fracture. However, it should be noted that the values of G_{IC} were in very close agreement for specimens both

with and without side grooves. Both TDCB configurations gave similar values of G_{IC} for a given BGT. The average value of G_{IC} was found to increase from 2600 J/m^2 at 0.25 mm bond gap to 5800 J/m^2 at 1.3 mm, and remain almost constant for larger bond gap thicknesses as shown in Fig. 5. The fracture energy variation with BGT of the adhesive appears to follow the theory put forward by [3], i.e. G_{IC} increases until the diameter of the plastic zone, r_p, under plane strain conditions, reaches the BGT and remains fairly constant afterwards, where;

$$r_p = \frac{1}{3\pi}\left(\frac{K_{Ic}}{\sigma_y}\right)^2 \tag{5}$$

and

$$K_{Ic}^2 = G_{Ic}\frac{E}{\left(1-\nu^2\right)}.$$

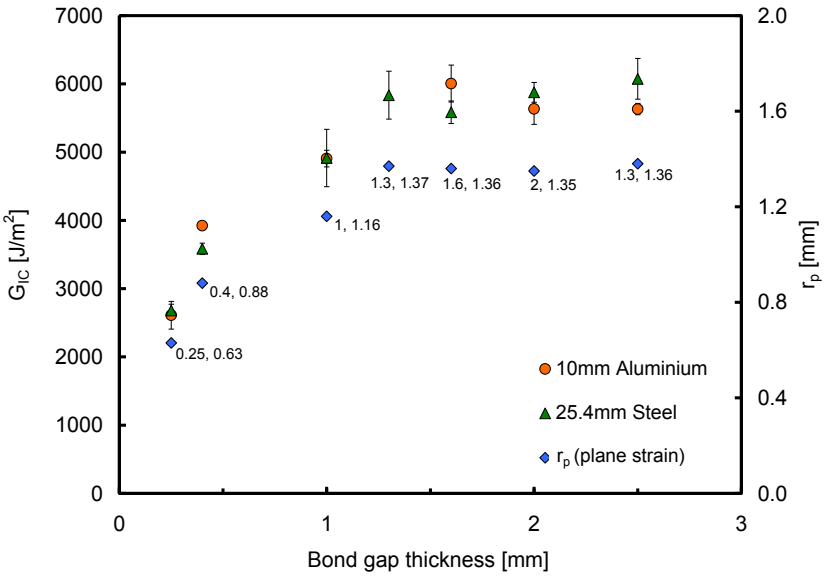

Fig. 5. Plot of G_{IC} versus BGT. Also shown are the average plastic zone sizes calculated for each corresponding BGT and G_{IC} using Eq. (5).

5.2 CDNT results

In parallel with TDCB tests, experiments were carried out using CDNT specimens with various LBA ratios and hence a variable level of constraint. It was originally intended to measure directly the entire TS curve and hence the main CZM parameters namely G_{IC} and

cohesive strength σ_{max}. However, it was not possible to generate values of G_{IC} from the CDNT experiments as the specimens failed in a rapid manner as soon as the peak stress was reached. Instead, CDNT tests only yielded acceptable values of σ_{max} as a function of constraint. Fig. 6a presents typical traction versus displacement traces for the three LBA ratios. Different LBA ratios resulted in different curves. As expected, lower LBA ratio, which corresponds to a higher level of constraint, results in a somewhat stiffer behaviour of the adhesive and in an increase in the peak stress. Good repeatability in the experimental results was achieved for all LBA ratios particularly with respect to the measured maximum tractions (Table 3). The surfaces of the failed ligaments of the CDNT specimens were reasonably uniform around the circumference, although some whitening around the notch indicated an increased level of plastic deformation in that region as compared to the rest of the ligament (Fig. 6b). It is however argued that CDNT tests resulted in a reasonable direct estimate of the cohesive strength σ_{max} as a function of constraint. This will be further examined via numerical simulations in Section 6.3; the value of σ_{max} used in the simulation that results in a good agreement between numerical and experimental traction-displacement curves is expected to be close to the experimentally measured maximum traction for each LBA. It should also be pointed out that the measured σ_{max} values are in good agreement with recently published results on a similar adhesive [49–51] where the complete TS curves were measured using the CDNT geometry.

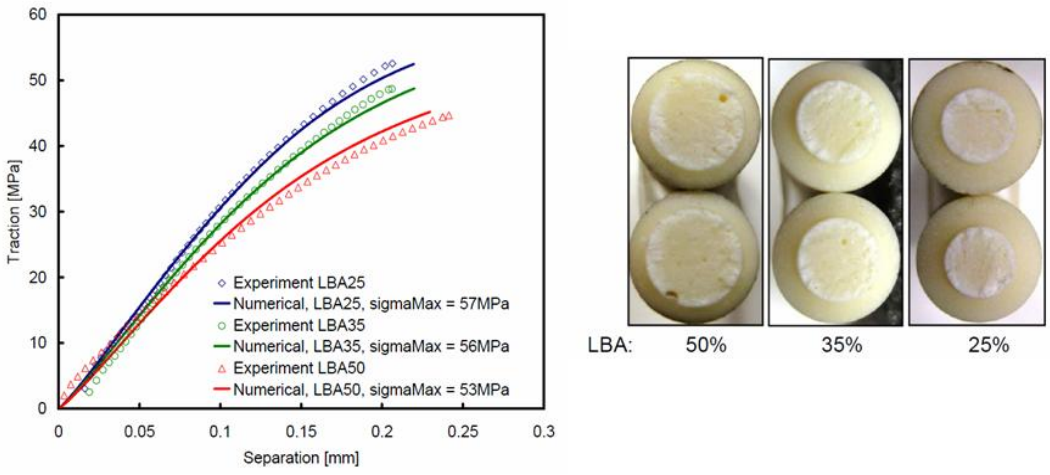

(a) (b)

Fig. 6. CDNT typical results: (a) traction vs. displacement curves for three LBA ratios. Also shown are numerical results which will be discussed in Section 6.3, (b) fracture surfaces.

Table 3. Scatter of σ_{max} from CDNT experiments. Peak values from results plotted in Fig. 6 are given in bold.

LBA [%]	σ_{max} [MPa]	**Mean** [MPa]	**Std. Dev.**
25	58.0	52.7	5.2
	47.6		
	52.6		
35	51.8	47.7	3.8
	47.4		
	48.7		
	42.7		
50	47.8	44.0	3.1
	40.4		
	42.9		
	44.7		

6.0 Finite volume modelling

6.1 Introduction

The finite volume (FV) numerical method was used to model the experiments by employing the 'OpenFOAM' software package [52]. The FV method incorporating various types of CZM has successfully been employed in modelling adhesive fracture [25,26,53–55]. In the current work an elastic-plastic material model based on classical incremental J2 flow theory with von Mises yield criterion was used to model both the substrates and the adhesive. A Dugdale type CZM was used to describe the mode I fracture in the adhesive. The traction-separation law is applied along a prospective crack path in the mid-plane of the adhesive. This type of law is initially rigid and therefore prospective cohesive surfaces behave in the same manner as the surrounding bulk material before the normal tractions on the surface reach the cohesive strength, i.e. the prospective crack is initially modelled as a symmetry plane. After the normal traction reaches σ_{max} representing the onset of damage, the corresponding cohesive surfaces of the adhesive behave according to the prescribed Dugdale traction-separation law. Due to symmetry, the cohesive face is assumed to be fractured when the normal separation of the cohesive face reaches half the critical value and the tractions are dropped to zero representing the free surface. The Dugdale CZM is defined by two material parameters, the adhesive fracture energy G_{IC} and the maximum cohesive stress σ_{max}. In the TDCB simulations, the value of G_{IC} was set equal to the corresponding experimental value while σ_{max} was assumed equal to the UTS measured from

the uniaxial tensile tests (Section 3.2). This choice was supported by CDNT experiments where σ_{max} was measured as a function of constraint for the adhesive [48,56]. The influence of the maximum cohesive stress and the fracture energy, on the predicted force-displacement and crack length curves was evaluated for both the TDCB and the bulk CDNT geometries [48]. In addition, the constraint factor, i.e. the stress triaxiality, was numerically quantified in the TDCB specimens along the crack front for various BGT and in CDNT across the ligament for various LBA ratios.

6.2 Modelling the TDCB test

Due to double symmetry, only quarter of the specimen was modelled. Both 2D plane strain and 3D simulations were performed. Special care was taken to ensure mesh independent results to within a level of uncertainty consistent with the experimental scatter. The constant test speed was achieved by applying a fixed displacement increment in each time step which was set to 1s. Fully implicit time discretisation was employed which ensured unconditional stability of the solutions for any time step size.

The results of the sensitivity study on the effects of G_{IC} and σ_{max} on the numerical predictions of both load and crack length vs. displacement traces for two BGTs are given in Fig. 7. Fig. 7a indicates that the numerical predictions for the geometry with the highest level of constraint, i.e. 0.25 mm BGT, were relatively insensitive to the value of σ_{max}. On the other hand, as the constraint decreases (BGT increases) the effects of σ_{max} become more pronounced, Fig. 7b. The numerical prediction of the experimental results for the BS TDCB geometry was strongly influenced and hence governed by the value of the fracture toughness. This is demonstrated in Fig. 8 which shows the effect of G_{IC} on the numerical predictions for 0.25 and 2 mm BGT. Similar conclusions were obtained for the ASTM TDCB geometry. Furthermore, it was found that the results for each of the TDCB experiments could be matched numerically using only a very narrow range of toughness values. In fact, the values of G_{IC} equal to the experimentally measured values consistently gave the closest agreement with experimental load and crack length traces in every case with σ_{max} = UTS. The force-displacement and crack length traces for the 10 mm wide TDCB tests are plotted in Fig. 9. A similar analysis was carried out for the wider ASTM type geometry. Again, excellent experimental-numerical agreement over the range of bond gap thicknesses was achieved.

6.3 Modelling the CDNT test

CDNT tests conducted at a crosshead velocity of 0.05 mm/min for the range of LBA ratios were also simulated numerically using the FV CZM procedure explained above. The aim was to investigate if the peak tractions directly measured from the CDNT test could be used as an approximation of the cohesive strength σ_{max}. One eighth of the specimen was modelled (although the problem is axisymmetric) and a constant test speed was applied. Since the specimens failed in a rapid manner once the peak stress was reached the behaviour of the CDNT specimens were only recorded and simulated before the fracture took place. The predicted initiation load was found to be mainly dominated by the cohesive strength while the variation in G_{IC} had minimal effects, only affecting the length of the load-displacement curve [48]. Hence, a constant value of G_{IC} = 2800 J/m^2 was used in the presented simulations of CDNT tests. When the value of σ_{max} is set to a constant value for each level of constraint (LBA ratio), the maximum predicted traction was also found to be constant and equal to σ_{max} and hence independent of LBA. However, this does not agree with what was observed experimentally. As the LBA ratio is decreased, there is a corresponding increase in the level of constraint and the cohesive strength. In order to simulate this and achieve good agreement with the experimental results, the value of σ_{max} used in the numerical simulations had to be varied with LBA. Fig. 6a gives the best-fit predicted curves compared with the experimental results. As expected, the higher the constraint, the higher the required σ_{max} value to fit the experimental results. The CZM parameters used in the simulations are summarised in Table 4 together with the experimental peak stress results. As expected, the numerical σ_{max} values are slightly higher than the experimentally measured values. This is due to the fact that the experimental σ_{max} values represent an average value of the stress across the ligament of the CDNT specimen which was not uniform [48]. However, it is thought that experimentally measured peak tractions are an acceptable approximation of cohesive strength σ_{max}, and further development of the CDNT test for the direct measurement of cohesive strength is currently being undertaken [49,51].

Table 4. Cohesive parameters used in the final CDNT simulations. G_{IC} = 2800 J/m^2.

LBA (%)	$\boldsymbol{\sigma_{max}}$ [MPa] numerical	$\boldsymbol{\sigma_{max}}$ [MPa] experimental	**% difference**
25	57	53	7
35	56	49	12
50	53	45	15

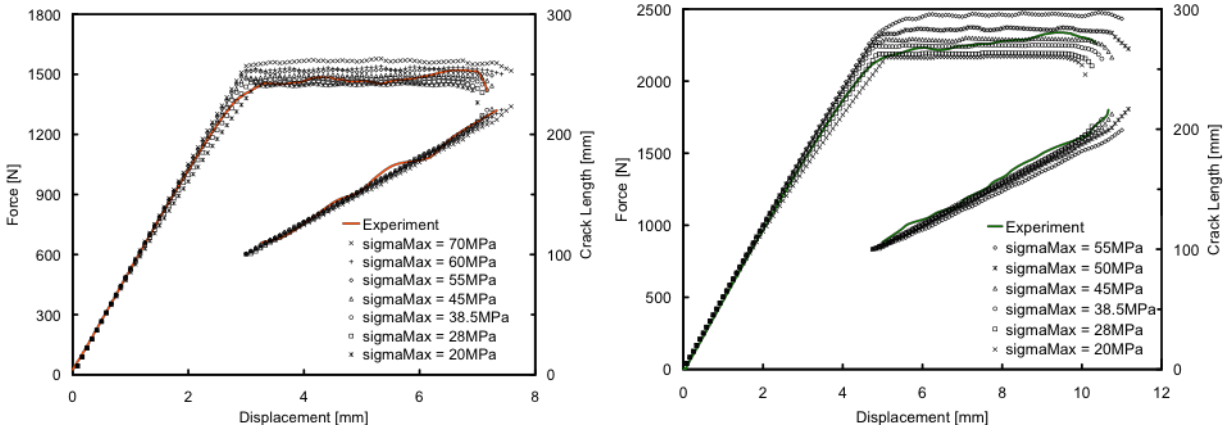

(a) (b)

Fig. 7. Effects of σ_{max} for BS TDCB: (a) 0.25 mm BGT (G_{IC} = experimental = 2610 J/m^2) and (b) 2 mm BGT (G_{IC} = experimental = 5900 J/m^2).

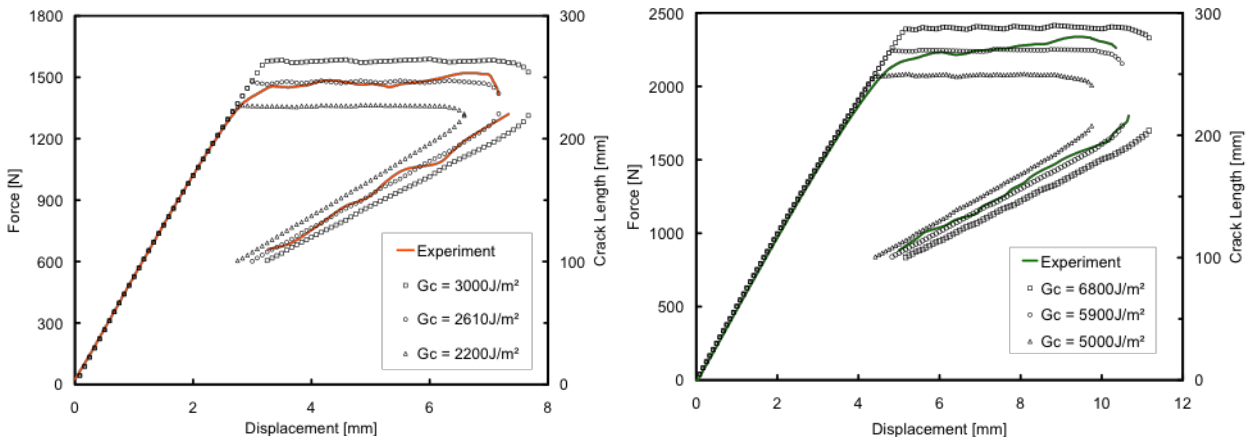

(a) (b)

Fig. 8. Effects of G_{IC} for BS TDCB with σ_{max} = UTS = 38.5 MPa: (a) 0.25 mm BGT and (b) 2mm BGT.

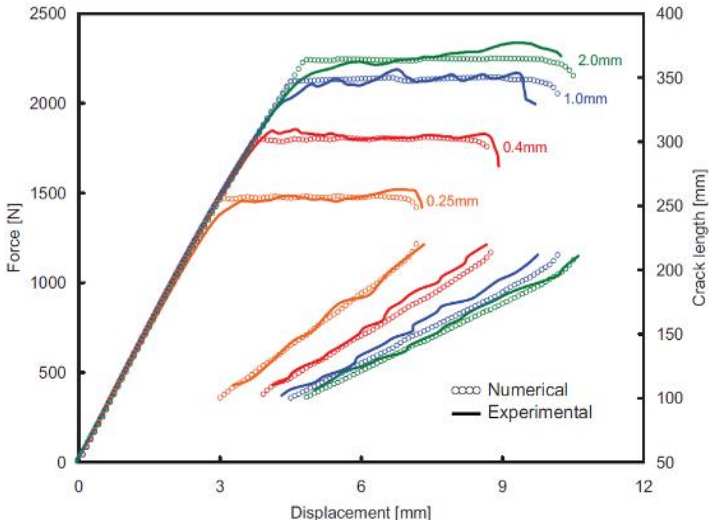

Fig. 9. Experimental load-displacement and crack length-displacement data and numerical predictions for 0.25 mm, 0.4 mm, 1.0mm and 2.0mm BGT cases (10 mm wide TDCB). G_{IC} = 2610 J/m^2, 3900 J/m^2, 5400 J/m^2 and 5900 J/m^2 respectively, σ_{max} = UTS.

6.4 Link between TDCB and CDNT via constraint (geometrical transferability)

In the current work, in accordance with the usual convention, the constraint factor *H* is used as a measure of the stress triaxiality. If the loading rate and temperature are fixed during testing, it is also conventional to assume that fracture (CZM) parameters are uniquely dependent on *H*. Hence, this factor could be used to link different test geometries, i.e. *H* becomes the geometrical transferability parameter. Here, an attempt is made to link cohesive strength values between TDCB and CDNT geometries using *H*. A similar approach could not be applied to G_{IC} as the CDNT test did not yield reliable values of fracture energy. On the other hand, the cohesive strength was measured directly using CDNT while it was extracted numerically for the TDCB geometry via a sensitivity analysis (Section 6.2, Fig. 7). *H* is defined as the ratio of the hydrostatic stress σ_{hyd} and the von Mises equivalent stress σ_{eq},

$$H = \frac{\sigma_{hyd}}{\sigma_{eq}} \tag{6}$$

where

$$\sigma_{hyd} = \frac{tr(\boldsymbol{\sigma})}{3} \tag{7}$$

and σ_{eq} can be expressed as:

$$\sigma_{eq} = \sqrt{3J_2} \tag{8}$$

where J_2 is the second invariant of the deviatoric stress tensor defined as:

$$J_2 = \frac{1}{2}[\boldsymbol{\sigma}_d : \boldsymbol{\sigma}_d] \text{ and } \boldsymbol{\sigma}_d = \boldsymbol{\sigma} - \sigma_{hyd}\mathbf{I} \tag{9}$$

Figs. 10a and 10b present the variation of H in TDCB and CDNT geometries, respectively. In each of the TDCB calculations given in Fig. 10a σ_{max} was assumed equal to the UTS measured from the tensile tests performed at a low rate. This is the stress at which the material will fail under uniaxial conditions, for which the constraint factor H = 1/3. In the crack tip region, $H \geq 1/3$ and hence the minimum separation stress is equal to the UTS. Assuming σ_{max} to be equal to the UTS value is a somewhat arbitrary choice and is based on the best-fit numerical sensitivity study. While numerical simulations of the TDCB specimens showed a strong sensitivity of the results to the value of G_{IC} (Fig. 8), the variations in σ_{max} had less pronounced effects (Fig. 7). Hence, this choice would not have a considerable effect on the calculation of H. On the other hand, CDNT results (prior to fracture) were strongly dependent on σ_{max} but not on the choice of G_{IC} (Fig. 6a). They also demonstrated a moderate dependency of σ_{max} on LBA and hence H (Table 4). Variation of H in both TDCB and CDNT geometries is calculated numerically at the instant of fracture initiation as a function of BGT and LBA, respectively.

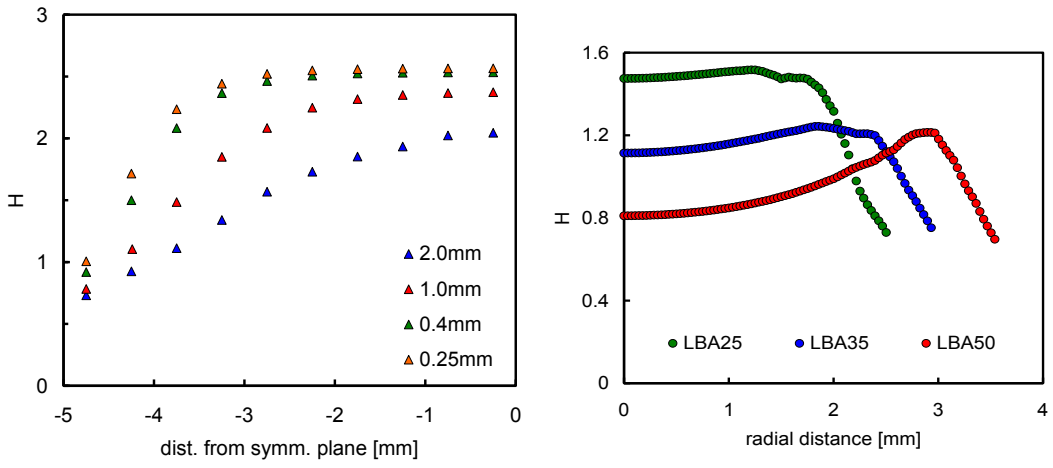

(a) (b)

Fig. 10. Computed values of H: (a) for TDCB as a function of BGT, (b) for CDNT as a function of LBA.

Fig. 10a shows the variation of *H* along half of the crack front (free surface to symmetry plane) as a function of BGT for TDCB geometry, while Fig. 10b illustrates the variation of *H* along the radial distance from the axis of symmetry to the free surface for the CDNT geometry as a function of LBA. Results shown for the TDCB are generally in agreement with those previously reported [10,57]. Also, the values of *H* for TDCB are generally higher than those of CDNT, e.g. in the middle of the samples *H* varies from 1.9 to 2.5 (as BGT varies from 2 mm to 0.25 mm) in the TDCB geometry and from 0.8 to 1.5 (as LBA varies from 50% to 25%) in the CDNT geometry. In order to obtain a single representative value of *H* for a given geometry so that appropriate functions of *H*, i.e. $\sigma_{max}(H)$ and $G_{IC}(H)$ can be established, the values of *H* are averaged along the TDCB crack front line for each BGT and along the meridian for the CDNT geometry for each LBA just prior to crack initiation [48]. It was found that *H* decreases from around 2.3 at BGT = 0.25 mm to approximately 1.4 at 2.5 mm BGT in the TDCB geometry, and from 1.3 at LBA25 to 1 at LBA50 for the CDNT geometry. Fig. 11 shows the variation of numerically calibrated σ_{max} as a function of *H* for both CDNT and TDCB geometries. The values for CDNT are taken from Table 4 and for TDCB are extracted from the σ_{max} sensitivity study (presented in Fig. 7 for two of the bond gap thicknesses). The TDCB σ_{max} is found to vary from the minimum value equal to UTS to the maximum value which gives a numerical prediction that lies within the variation of the experimental load-displacement results (Fig. 7). It can be seen from Fig. 11 that the level of constraint in CDNT geometry has not reached that of TDCB for the LBA ratios considered and hence the CDNT *H* values lie below the TDCB *H* values. Also, CDNT $\sigma_{max}(H)$ is an upper bound of the TDCB results, but the agreement is at the very least encouraging. The results presented in Fig. 11 provide a link between the two very different geometries and more importantly give the variation of σ_{max} with *H*, backed up by experimental measurements.

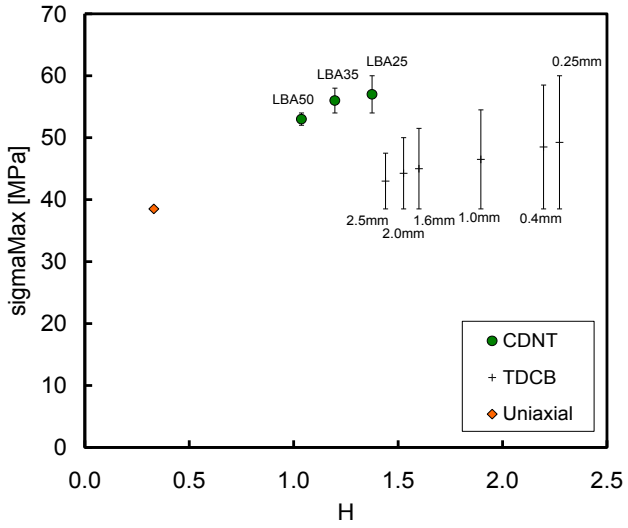

Fig. 11. Variation of σ_{max} with *H* for CDNT and TDCB geometries.

In Fig. 12a the values of G_{IC} obtained from the TDCB tests from Fig. 5 are re-plotted against BGT together with the corresponding values of *H*. It can be seen that the fracture energy plateaus approximately when the constraint begins to level off, i.e. stops changing appreciably with BGT. The vertical dashed line in Fig. 12a corresponds to the point beyond which G_{IC} becomes independent of *H*. Fig. 12b shows G_{IC} as a function of *H*. At values of *H* below approximately 1.6, as indicated by the dashed line, G_{IC} remains constant and equal to almost 6 kJ/m^2. Above *H* = 1.6, a strong dependence of G_{IC} with *H* can be seen where G_{IC} drops to approximately 2.5 kJ/m^2 at *H* = 2.3. In conclusion, the dependency of σ_{max} and G_{IC} with the constraint factor *H* have been demonstrated, as well as the transferability of σ_{max} between CDNT and TDCB via *H*.

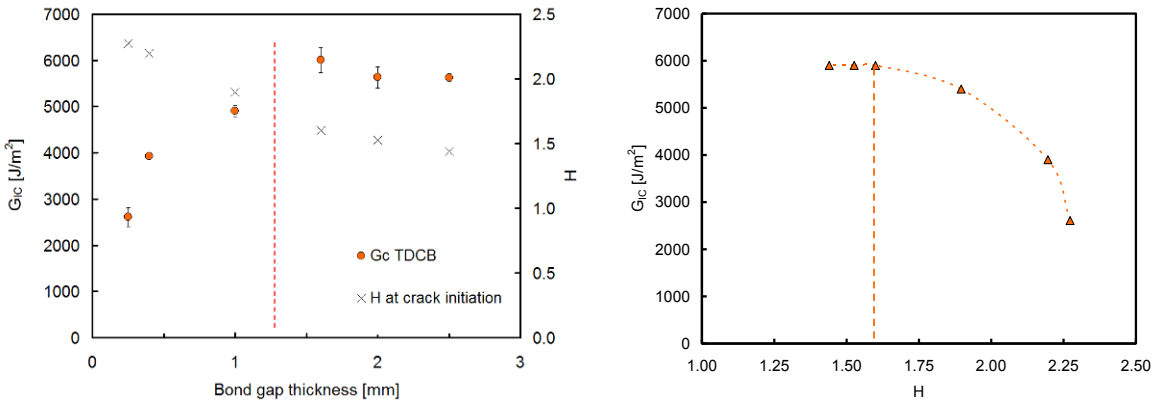

(a) (b)

Fig. 12. Variation of fracture energy in TDCB test (a) G_{IC} and *H* vs. BGT, (b) G_{IC} vs. *H.*

7.0 Discussion on G_{IC} dependence on the bond gap thickness

It can generally be assumed that:

$$G_{IC} = G_{IC}\left(\dot{\varepsilon}, H, T\right) = G_O\left(\dot{\varepsilon}, H, T\right) + G_P\left(\dot{\varepsilon}, H, T\right) \quad (10)$$

where $\dot{\varepsilon}$ is the strain rate, H the measure of constraint, T temperature, G_o the intrinsic work of fracture resulting from the separation processes in the fracture process zone (FPZ) and represented by the cohesive separation energy, and G_P the contribution to total fracture energy from the far-field plastic dissipation within the adhesive layer but outside FPZ. In the current work, both strain rate and temperature were kept fixed and hence G_{IC} is expected to be a function of constraint only. Different BGTs will introduce different levels of constraint in the adhesive, and the G_{IC} dependence on H can be explained by considering one of the approaches summarised in Table 5.

Table 5. Various approaches to explain G_{IC} vs. BGT.

Approach	$G_{IC}(H)$=
1	$G_P(H)$
2	G_O+$G_P(H)$
3	$G_O(H)$
4	$G_O(H)$ +$G_P(H)$

Approach 1 is based on the classical argument that the size of the plastic zone in the adhesive layer is physically restricted by the two 'rigid' substrates and hence G_{IC} dependency on BGT (see Section 1.0) [3]. The effects of constraint H within the adhesive layer are not accounted for, only the physical proximity of the substrates. This approach is based on the Irwin estimate of the plastic zone size and any contribution arising from the FPZ is embedded into G_P. Based on Fig. 5, it appears that the fracture energy dependence on BGT of the current adhesive follows this approach as G_{IC} plateaus when the Irwin estimate of the plastic zone diameter r_P under plane strain conditions reaches the BGT at 1.36 mm. However, this is not surprising as the calculation of r_P (Eq. (5)) is based on already determined values of G_{IC} which plateaus at BGT = 1.3 mm. It should also be pointed out that the Irwin estimate of r_P is only valid if a K dominant stress field exists near the crack tip. However, this assumption is not satisfied in the current TDCB experiments whose results are presented in Fig. 5 [56]. Numerical simulations of the TDCB experiments presented in Section 6.2 revealed only a very small level of plastic dissipation near the free surfaces of the specimens [48,56] and the results did not support the approach 1 argument. The

simulations however, allowed for the competition between damage-fracture and plasticity, and the low ratio of cohesive strength to yield stress (σ_{max}/σ_y) used in the analysis favours the development of damage and eventual fracture over plasticity [30]. In most reported literature σ_{max} is taken as infinite, i.e. the damage was not accounted for e.g. [9,10], or σ_{max} is assumed to be much higher than the yield stress [8,19] resulting in large plastic dissipation in the adhesive layer. It is important to point out that no direct experimental evidence was offered to verify the choice of high σ_{max}. In only a limited number of publications, a direct measurement of the plastic zone size was achieved but only in bulk adhesive specimens where good comparison with Irwin plasticity is reported [58,59]. These measurements were based on polarised light transmission optical microscopy (TOM) and while the overall size of the 'damaged' region could be measured no distinction was made between FPZ and far-field plasticity.

Approach 2 is an extension of approach 1. It partitions G_{IC} into a local intrinsic contribution G_0 coming from the FPZ and a non-local contribution G_P [8,28]. In [8] and [28], G_0 is kept fixed and hence the variation in G_{IC} with BGT is solely attributed to the variation in G_P with BGT. A constant G_0 would suggest that the fracture process zone and fracture features are uniform and do not change with BGT. In the current work this was not found to be the case as will be shown later in this section. The main problem with this approach is the choice of G_0 which is not known in advance as the size of FPZ is not known. As G_0 is fixed for all BGTs one can assume that the smallest bond gap thickness with the smallest G_P contribution should yield the closest value for G_0. Ideally, if this thickness happens to coincide with the size of the FPZ then a correct G_0 should be obtained. In [8] and [28], the cohesive strength was taken to be greater than three times the adhesive yield stress and G_0 was extracted from numerical steady-state simulations of a set of wedge peel tests for two different adhesives [19]. The validity of this approach was argued on the basis of reasonably good comparison with compact tension and TDCB results, and good prediction of bond gap dependence of G_{IC} in wedge peel tests. However, good prediction of G_{IC} vs. BGT dependence does not guarantee the correct choice of G_0. Stemming from the energy balance, any value of G_0 must result in G_P such that predicted $G_0 + G_P$ is equal to the experimental G_{IC} (for all BGT greater than the one that yields the value of G_0) provided that the experimental fracture load is matched. To demonstrate this, the results shown in Fig. 5 were predicted using two different values of G_0: i) 2600 J/m^2 which corresponds to the smallest tested BGT

of 0.25 mm and ii) 3600 J/m^2 which corresponds to the next smallest tested BGT of 0.4 mm (this value was chosen arbitrarily for the purpose of the exercise). σ_{max} was varied until the experimental load vs. displacement data were reproduced numerically; σ_{max} = 80 MPa was required for G_0 = 2600 J/m^2 and σ_{max} = 72 MPa for G_0 = 3600 J/m^2. Fig. 13a shows the comparison between numerical and experimental load vs. displacement and crack length vs. displacement results for BGT = 2 mm. Both linear elastic and elastic plastic analyses were performed. The difference between predictions from these two analyses indicates the value of the load required for generating G_P (Fig. 13a), which is calculated as:

$$G_P = \frac{dW_P}{dA}. \tag{11}$$

where plastic work W_P is given as:

$$W_P = \int_{V_P} \omega_P dV \text{ and } \omega_P = \int_{\varepsilon_P} \boldsymbol{\sigma} : d\boldsymbol{\varepsilon}^p \tag{12}$$

$dA = Bda$ is the increment of fracture area, ω_P plastic energy density, V_P volume of plastically deformed material and $\boldsymbol{\varepsilon}^P$ plastic strain tensor.

Fig. 13b shows the experimental G_{IC} vs. BGT results together with numerical predictions using G_0/σ_{max} = 2600/80 and 3600/72 [J/m^2/MPa]. It can be seen that when approach 2 is employed the experimental data can be reproduced using different G_0/σ_{max} values, i.e. there is no unique combination of G_0 + G_P. It is worth mentioning that the higher σ_{max}/σ_y allows a larger plastic zone to develop.

Approach 2 is found to be inappropriate for the adhesive tested in this work for a number of reasons: i) G_0 cannot be assumed fixed for different BGT as different features were observed on the fracture surfaces of joints with different BGT (see void size argument later in this Section), ii) σ_{max} required to match the experimental load traces is too high compared to the experimental data and iii) the prediction of crack length traces are not as accurate as those using approach 3 and presented in Fig. 9. It should also be pointed out that smaller G_0/σ_{max} ratios, i.e. smaller crack opening displacement (COD), led to numerical instabilities represented by characteristic stick-slip load traces.

As presented in Sections 6.1 and 6.2 and summarised in Fig. 9, the TDCB tests on the current adhesive were best reproduced in terms of both load and crack length traces predictions using approach 3. Intrinsic G_0, represented by CZM, is taken to be equal to the total

experimental G_{IC} for different values of BGT or *H,* while σ_{max} was kept constant and equal to measured UTS of the adhesive. Only a small level of plastic dissipation near the free surfaces of the specimens was predicted and this was not accounted for in the calculation of total G_{IC}. It would be more appropriate to reduce the CZM separation energy by the corresponding plastic dissipation contribution, i.e. to use approach 4 as recently done by [50,51], but for all practical purposes the assumption that $G_0(H) = G_{IC}(H)$ suffices.

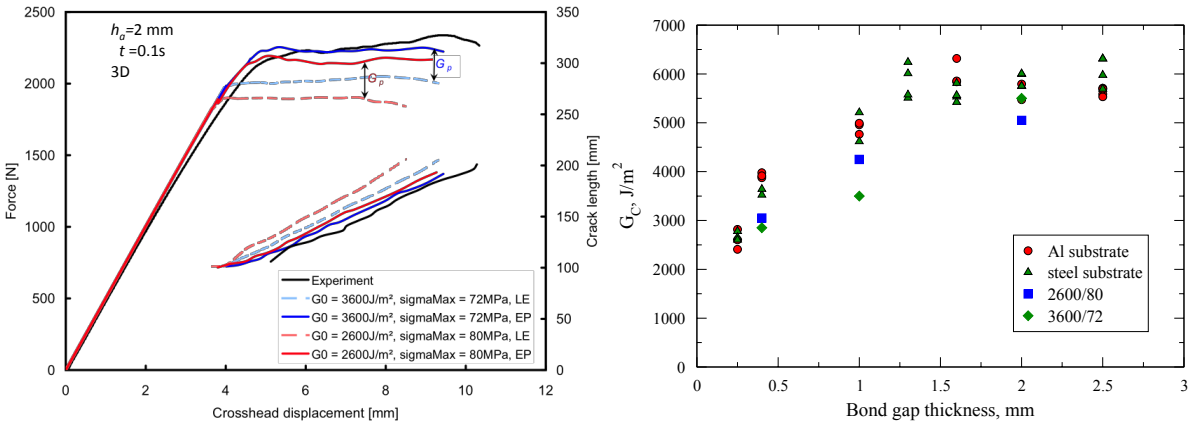

Fig. 13. Non-uniqueness of approach 2, (a) Force and crack length vs. displacement, (b) G_{IC} vs. *BGT.*

The question however remains of how to quantitatively explain the variation in G_{IC} as a function of BGT (or *H*). To address this, one needs to look more closely into the damage and toughening mechanisms in the adhesive, i.e. the structure-property relationship. According to approach 3, which was shown to be most appropriate for the adhesive studied in this work, the constraint affects the intrinsic fracture toughness and hence the FPZ, i.e. the effects of the BGT on G_{IC} mainly comes from the constraint effects on G_0. If this is the case, it should be possible to obtain some evidence of the effect of constraint on G_0 from the fracture surfaces. The toughening of the current adhesive is achieved through the addition of core shell nano-particles and the main toughening mechanisms are thought to be plastic void growth following the debonding of these particles from the epoxy matrix and the development of shear bands [58–60]. Evidence of void growth was clearly observed on the fractured surfaces while no direct evidence of shear bands was found for the tested adhesive. In the authors' opinion, there is no direct convincing evidence of shear bands reported in the literature for nano-toughened adhesives on the nano scale. For example, the micrographs obtained under cross-polar TOM in [58–60] are of the order of 50 to 100 μm

scale and they show the overall plastic zone where 'alleged' nano-size shear bands cannot be distinctively observed. On the other hand, micro-scale shear bands are clearly shown in a number of publications e.g. [59]. In addition, an attempt was made to calculate the overall toughness of the adhesive using the classical Huang and Kinloch model [61,62] which estimates the absorbed energy through the void growth and shear banding separately [50]. It was found that the contributions from the unmodified neat epoxy matrix and plastic void growth toughness closely matched the experimental G_{IC} results and the addition of a shear band contribution led to an overestimation of the experimental results. Hence, it is assumed that the main energy absorbing mechanism in the current adhesive is due to the plastic void growth. This assumption is however not critical for the arguments and conclusions made below.

A detailed analysis of the TDCB fracture surfaces was carried out using scanning electron microscopy (SEM) and variations of the microstructural features with BGT were examined. Of particular interest is the size of the voids at different levels of constraint. The Rice and Tracey void growth model [11] was used to relate the local plastic strain, calculated by measuring the size of the voids on the fracture surfaces, with the constraint calculated numerically for each BGT. Under the assumption of spherical void growth in a perfectly plastic material and a constant critical void radius, the ratio of two fracture strains, ε_{f1} and ε_{f2}, at different constraints, H_1 and H_2, according to the Rice and Tracey model is given by:

$$\frac{\varepsilon_{f1}}{\varepsilon_{f2}} = e^{1.5(H_2 - H_1)} \tag{13}$$

The above assumptions are thought to be reasonably adequate for the adhesive considered in this work. The stress strain curve in Fig. 1 shows almost perfect plasticity for strains above 5%. The ratio of final void diameters as observed on the fracture surfaces varied from 6% for BGT of 1.6 and 0.4 mm to 19% for BGT of 2 and 0.4 mm (see Table 6). This ratio was small compared to the ratio of strains which was around 3 for BGT of 2 and 0.4 mm as will be shown later. The strain can be approximated as:

$$\varepsilon_f = \frac{u_r}{r_0} \tag{14}$$

where u_r is the final radial displacement of the void and r_0 is the original radius of the void (particle size).

For illustration purposes, the detailed analysis of two 10 mm wide fractured TDCB specimens corresponding to bond gap thicknesses of 0.4 mm (G_{IC} = 3830 J/m^2) and 2.0 mm (G_{IC} = 6007 J/m^2) are presented here. Combining Eq. (13) and Eq. (14) it follows that:

$$\frac{\varepsilon_{f(0.4)}}{\varepsilon_{f(2.0)}} = \frac{u_{r(0.4)}}{u_{r(2.0)}} = \frac{r_{(0.4)} - r_0}{r_{(2.0)} - r_0} = e^{1.5(H_{(2.0)} - H_{(0.4)})} \tag{15}$$

where subscripts (0.4) and (2.0) were used to denote values at 0.4 mm and 2.0 mm BGT, e.g. $r_{(0.4)}$ and $r_{(2.0)}$ are the final radii of the voids from the 0.4 mm and the 2.0 mm BGT tests, respectively. Firstly, a batch of the larger particles in their original powder form was gold sputter coated and viewed under SEM. The particle diameters were recorded using a Java-based image processing and analysis program called ImageJ [63]. The same batch of particles then underwent a second gold coating cycle and the diameters were measured again. The difference between the mean radius for both sets of measurements is the gold coating thickness, and the particle size distribution was determined by subtracting the total gold coating thickness from every measurement. The average particle radius, r_0 ,was found to be 100.4 nm with a standard deviation of 14 nm.

Segments of the TDCB fracture surfaces were also coated prior to SEM imaging. All voids were selected from one quarter of the micrograph (boxed region in Fig. 14) and the diameters were measured and averaged. The average void radius was calculated to be 104 ± 14 nm for the 0.4 mm sample and 125 ± 14 nm for the 2.0 mm sample. The standard deviation of the void sizes closely agreed with the standard deviation of the particle distribution and the minimum void diameter found was 100nm indicating that all measured voids correspond to debonding of the larger particles. In total, four representative bond gap thicknesses were analysed using this method and the results were given in Table 6 (due to time, facility and financial constraints only 4 BGT were selected but this is not thought to have an influence on the outcome of the analysis).

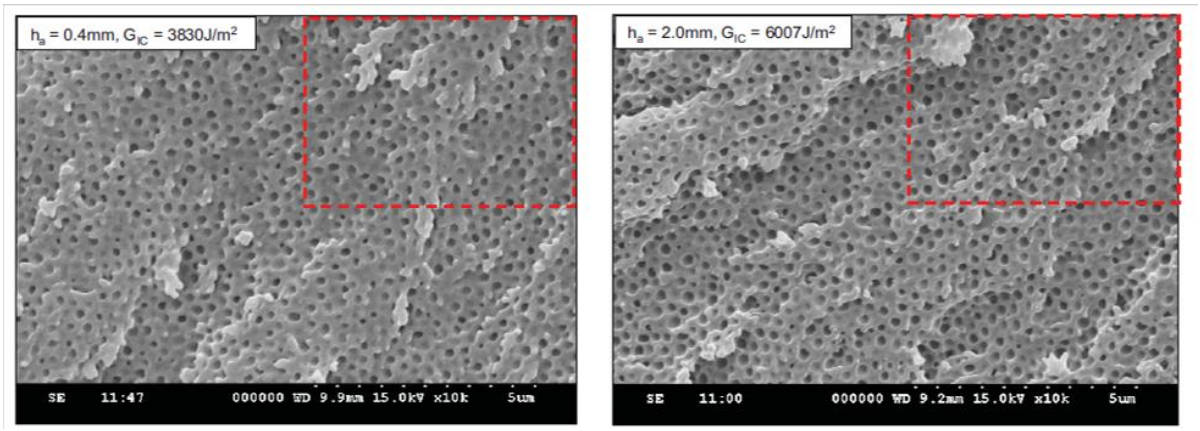

(a) (b)

Fig. 14. Micrograph (x10k) taken from the fracture surface of (a) 0.4 mm and (b) 2.0 mm BGT specimens.

The difference in the stress triaxiality between the two bond thicknesses, i.e. $H_{(2.0)} - H_{(0.4)}$, at the crack-tip region just prior to crack initiation is 1.53 − 2.2 = −0.67 giving the value of the RHS of Eq. (13) equal to 0.37. To calculate the ratio of fracture strains, the final void radius was corrected for the thickness of the gold coating deposited on the fracture surface. Although the coating thickness on the TDCB surfaces was not measured there is an established lower bound for gold coating thickness of 6nm and an upper estimate for thickness can be made based on the deposition process parameters [64] using the following empirical equation:

$$T = \frac{CVtK}{10} = \frac{20 \times 2.4 \times 3 \times 0.7}{10} = 10.1 \tag{16}$$

where T is the coating thickness in nm, V in keV, C is the discharge current in mA, t is the deposition time in minutes and K is a constant depending on the target material and bombarding gas. The ratio of fracture strains can then be determined based on a gold coating thickness range of 6-10 nm where $\varepsilon_{f(0.4)}/\varepsilon_{f(2.0)}$ = 0.32-0.39, or the 2.0 mm BGT strain is close to 3 times larger than that of the 0.4 mm BGT.

Taking the average coating thickness to be 8nm the values of $\varepsilon_{f1}/\varepsilon_{f2}$ for each combination of bond gap thicknesses (from Table 6) were plotted against the corresponding $e^{(1.5(H2-H1))}$ and compared against the analytical Rice and Tracey prediction (Fig. 15). The results indicate a reasonable overall agreement. Table 7 gives the summary of average G_{IC} for four different BGT (and H) and corresponding ε_f. It can be seen that plastic strains at failure closely follow the variation in G_{IC} vs. BGT and H. As the bond gap thickness increases, the constraint level

within the adhesive decreases which allows for the increase in plastic void growth. This again indicates that the plastic void growth is mainly responsible for the toughening and variation of fracture toughness with bond gap thickness.

Table 6. Average measured void radii (i.e. $r_0 + u_r$) for various bond gap thicknesses.

BGT [mm]	*Particles*	*0.4*	*1.6*	*2.0*	*2.5*
Radius [nm]	100.4	104	111	125	117
Std. dev. [nm]	14	14	19	14	18

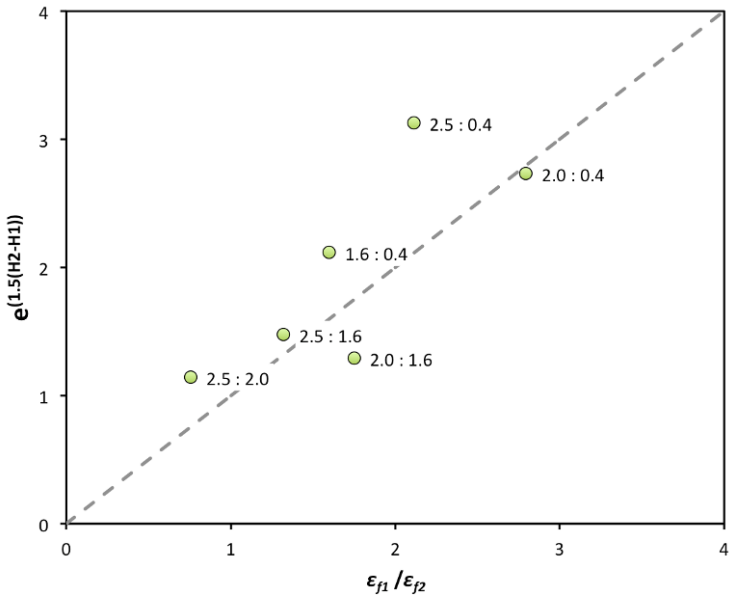

Fig. 15. Comparison of experimental results with the Rice and Tracey analytical solution for four bond gap thicknesses: 0.4 mm, 1.6 mm, 2.0mm and 2.5 mm with a gold coating thickness of 8nm.

Now, one can finally attempt to answer the question posed earlier in the section. The large differences in the plastic strains for the two bond gap thicknesses (factor of almost 3) as caused by the difference in constraint can be used to explain the differences in the corresponding fracture toughness. The fracture toughness can be approximated as:

$$G_{IC} \approx \sigma_f \varepsilon_f \delta_{FPZ} = \omega_P \delta_{FPZ} = \sigma_f \cdot COD \tag{17}$$

where σ_f is a fracture stress equivalent to cohesive strength (σ_{max}), ε_f fracture strain, δ_{FPZ} thickness of the fracture process zone, ω_P plastic energy density and *COD* crack opening displacement. Hence the ratio between fracture toughness's at two different BGT (2.0 and 0.4 mm) can be expressed as:

$$\frac{G_{IC(2.0)}}{G_{IC(0.4)}} = \frac{\sigma_{f(2.0)}\delta_{FPZ(2.0)}}{\sigma_{f(0.4)}\delta_{FPZ(0.4)}} e^{1.5(H_{(0.4)}-H_{(2.0)})}, \quad (18)$$

and by entering the range of values for parameters in Eq. (18), one obtains:

$$\frac{G_{IC(2.0)}}{G_{IC(0.4)}} = \left(\frac{38.5}{38.5} \text{ or } \frac{50}{60}\right)\frac{\delta_{FPZ(2.0)}}{\delta_{FPZ(0.4)}} 2.7 = (2.7 \text{ or } 2.25)\frac{\delta_{FPZ(2.0)}}{\delta_{FPZ(0.4)}} \quad (19)$$

This is based on values shown in Fig. 11 where the range of cohesive strengths varies from 38.5 to 50 MPa for a BGT of 0.4 mm and from 38.5 to 60 MPa for a BGT of 2.0 mm. The ratio of measured $G_{IC(2.0)}$/ $G_{IC(0.4)}$ = 1.58 and from Eq. (19) it follows that $\delta_{FPZ(2.0)}/\delta_{FPZ(0.4)}$ is between 0.6 and 0.7. It is somewhat surprising that the fracture process zone for the BGT of 2.0 mm and G_{IC} = 6 kJ/m^2 is smaller than that of BGT = 0.4 mm and the much lower G_{IC} of 3.6 kJ/m^2. However, the plasticity density ω_p for BGT = 2.0 mm is 14 to 18 MPa compared to only 5 to 8 MPa for BGT = 0.4 mm due to larger plastic strains in the small constraint BGT. A similar observation was made in [60] where the adhesive with the smallest plastic zone size was reported to have the largest fracture toughness. This also agrees with the recent work of [65] where toughening mechanisms of a nano-modified adhesive were investigated. It was shown that the size of the plastic region was less important than the intensity of plasticity. Their model indicated that the major source of energy absorption is located within a region of around 150 µm from the crack tip which was much smaller than the total size of the plastic zone.

Table 7. Average G_{IC} and ε_f for various bond gap thicknesses.

BGT [mm]	*0.4*	*1.6*	*2.0*	*2.5*
G_{IC} [kJ/m^2]	2.6	5.8	5.7	5.9
ε_f [%]	11.6	18.6	32.9	24.6
H	2.2	1.7	1.5	1.4

8.0 Conclusions

The mode I fracture behaviour of a nano-toughened structural epoxy adhesive manufactured by Henkel was examined using TDCB specimens. All tests were conducted at low loading rates and at room temperature on joints with various bond gap thicknesses ranging from 0.25 mm to 2.5 mm. Two TDCB configurations were used: *(i)* according to the ASTM protocol with steel substrates of 25.4 mm width and *(ii)* according to the BS protocol with 10 mm wide aluminium substrates. For joints with BGT around and above 1 mm, side grooves were machined on the sides of the specimens. Both configurations resulted in

comparable values of G_{IC} for a given bond gap thickness. The average value of G_{IC} was found to increase steadily from 2600 J/m^2 at 0.25 mm bond gap thickness to 5800 J/m^2 at 1.3 mm and remained nearly constant for larger bond gap thicknesses. In parallel with TDCB tests, experiments were carried out using CDNT specimens with various ligament to bulk area ratios which resulted in a variable level of constraint (*H*). The value of *H* was estimated numerically and was found to vary from around 1 at LBA50 to 1.3 at LBA25. The corresponding average values of the cohesive strength, σ_{max}, measured from CDNT tests varied between 44 MPa at *H* = 1 to 53 MPa at *H* = 1.3. Numerical simulations of the CDNT tests yielded somewhat higher values of σ_{max}, between 53 MPa at *H* = 1 to 57 MPa at *H* = 1.4. The simulations of the TDCB tests resulted in a higher range of *H*, i.e. the constraint factor *H* was found to increase from around 1.4 at 2.5 mm BGT to approximately 2.3 at BGT = 0.25 mm. Values of σ_{max} measured from CDNT tests were found to be in reasonable agreement with the numerically predicted σ_{max} as a function of constraint from TDCB tests. Hence, geometrical transferability of the cohesive strength between the TDCB and CDNT specimens was achieved by using *H*.

In the numerical analysis, which employed OpenFOAM, the Finite Volume based open source package, the fracture process was modelled by a conventional Dugdale shape CZM. The experimental TDCB results for each BGT were best reproduced when the intrinsic fracture energy, i.e. the area under the traction-separation law, was set equal to the corresponding experimental value of G_{IC}, and measured *UTS* used as the cohesive strength. A unique relationship between the fracture energy and the constraint level was established. The effect of BGT on the fracture behaviour of TDCB joints was hence directly attributed to the variation of intrinsic fracture energy with constraint and not to the variation of 'far field' plastic zone size with BGT as is conventionally assumed. Furthermore, numerical simulations revealed only small plastic deformation near the free sides of the TDCB specimens. This was caused by the relatively small ratio of cohesive strength σ_{max} (38 MPa) and the yield stress σ_y (28 MPa). Under the current test conditions this ratio is required to be around 3 and above for plane strain 'Irwin' plasticity to develop. Numerical simulations with higher values of σ_{max} did not yield satisfactory results compared to the experimental results. Even though the experimental force versus displacement data could be reproduced, the crack was predicted to initiate much sooner in the model than in the experiment. However, such high σ_{max} values could not be supported experimentally.

A detailed analysis of the fracture surfaces using SEM revealed variations of the micro-structural features with BGT and hence constraint. The void diameters on the TDCB fracture surfaces were measured and the fracture strain was estimated for different bond gap thicknesses. The results were found to follow the Rice and Tracey void growth model as a function of constraint. Finally, the Rice and Tracey model was employed to explain quantitatively the variation of G_{IC} with constraint and hence with BGT. It was argued that most of the deformation (and energy dissipation) occurs locally in the fracture process zone and that the intensity of local plasticity is the key factor in determining the fracture energy and not only the size of the fracture process region.

Acknowledgments

The authors wish to acknowledge the funding and support received from Henkel Ireland and the Irish Research Council for Science Engineering and Technology (IRCSET).

References

[1] W.D. Bascom, R.L. Cottington, R.L. Jones, P. Peyser, J. Appl. Polym. Sci. 19 (1975) 2545-2562.

[2] D.B. Lee, T. Ikeda, N. Miyazaki, N.S. Choi, Transactions of the ASME J. Eng. Mat. Tech. 126 (2004) 14-18.

[3] A.J. Kinloch, S.J. Shaw, J. Adhes. 12 (1981) 59-77.

[4] D.L. Hunston, A.J. Kinloch, S.S. Wang, J. Adhes. 28 (1989) 103-114.

[5] S. Mostovoy, E.J. Ripling, C.F. Bersch, J. Adhes. 3 (1971) 125-144.

[6] A.J. Kinloch, Adhesion and Adhesives: Science and Technology, Chapman and Hall, 1987.

[7] L.F. Kawashita, A.J. Kinloch, D.R. Moore, J.G. Williams, Int. J. Adhes. Adhes. 28 (2008) 199-210.

[8] T. Pardoen, T. Ferracin, C.M. Landis, F. Delannay, J. Mech. Phys. Solids 53 (2005) 1951-1983.

[9] S. Azari, M. Papini, J.K. Spelt, Eng. Fract. Mech. 78 (2011) 153-162.

[10] S. Azari, M. Papini, J.K. Spelt, Eng. Fract. Mech. 78 (2011) 138-152.

[11] J.R. Rice, D.M. Tracey, J. Mech. Phys. Solids 17 (1969) 201-217.

[12] Q.D. Yang, M.D. Thouless, Int. J. Fract. 110 (2001) 175-187.

[13] B.F. Sorensen, Acta Mater. 50 (2002) 1053-1061.

[14] B.R.K. Blackman, H. Hadavinia, A.J. Kinloch, J.G. Williams, Int. J. Fract. 119 (2003) 25-46.

[15] H. Yuan, Y. Xu, Comp. Mat. Sci. 43 (2008) 146-156.

[16] V. Tvergaard, J.W. Hutchinson, J. Mech. Phys. Solids 44 (1996) 789-800.

[17] Q.D. Yang, M.D. Thouless, S.M. Ward, J. Mech. Phys. Solids 47 (1999) 1337–1353.

[18] K.S. Madhusudhana, R. Narasimhan, Eng. Fract. Mech. 69 (2002) 865-883.

[19] T. Ferracin, C.M. Landis, F. Delannay, T. Pardoen, Int. J. Solids Struct. 40 (2003) 2889-2904.

[20] S. Li, M. Thouless, A. Waas, J. Schroeder, P. Zavattieri, Eng. Fract. Mech. 73 (2006) 64-78.

[21] A. Pirondi, in:, Proceedings of the 15th European Conference of Fracture, Stockholm, Sweden, 2004.

[22] C. Sun, M.D. Thouless, A.M. Waas, J.A. Schroeder, P.D. Zavattieri, Int. J. Solids Struct. 45 (2008) 3059-3073.

[23] C. Sun, M.D. Thouless, A.M. Waas, J.A. Schroeder, P.D. Zavattieri, Int. J. Solids Struct. 45 (2008) 4725-4738.

[24] S. Li, M.D. Thouless, A.M. Waas, J.A. Schroeder, P.D. Zavattieri, Composites Sci. Tech. 65 (2005) 281-293.

[25] I. Georgiou, A. Ivankovic, A.J. Kinloch, V. Tropsa, in:, Fract. Polym. Compos. Adhes. II, 2003, pp. 317-328.

[26] V. Cooper, A. Ivankovic, A. Karac, in:, Proceedings of the 31st Annual Meeting of the Adhesion Society, Austin, Texas, 2008, pp. 21-23.

[27] I. Georgiou, PhD Thesis, Imperial College London (2003).

[28] P. Martiny, F. Lani, A.J. Kinloch, T. Pardoen, Int. J. Adhes. Adhes. 28 (2008) 222-236.

[29] W. Brocks, ESIS Newsletter 40 (2004) 21-30.

[30] V. Tvergaard, J.W. Hutchinson, J. Mech. Phys. Solids 40 (1992) 1377-1397.

[31] N. Murphy, A. Ivankovic, Engineering Fracture Mechanics 72 (2005) 861-875.

[32] J. Koplik, A. Needleman, Int. J. Solids Struct. 24 (1988) 835-853.

[33] J. Kim, X. Gao, T.S. Srivatsan, Eng. Fract. Mech. 71 (2004) 379-400.

[34] T. Pardoen, J.W. Hutchinson, J. Mech. Phys. Solids 48 (2000) 2467-2512.

[35] T. Siegmund, W. Brocks, Int. J. Fract. 99 (1999) 97-116.

[36] T. Siegmund, Eng. Fract. Mech. 67 (2000) 139-154.

[37] I. Scheider, Eng. Fract. Mech. 76 (2009) 1450-1459.

[38] S.K.M. Ting, J.G. Williams, A. Ivankovic, Polym. Eng. Sci. 46 (2006) 763-777.

[39] S.K.M. Ting, J.G. Williams, A. Ivankovic, Polym. Eng. Sci. 46 (2006) 778-791.

[40] ISO 25217, (2009).

[41] ISO 527-2:1996, (1996) 1-14.

[42] ASTM D 3433, Annual Book of ASTM Standards (1999).

[43] BS 7991, British Standard Institution (2001).

[44] B.R.K. Blackman, H. Hadavinia, A.J. Kinloch, M. Paraschi, J.G. Williams, Eng. Fract. Mech. 70 (2003) 233-248.

[45] K.C. Pandya, J.G. Williams, Plast. Rubber Compos. 29 (2000) 439-446.

[46] S.K.M. Ting, PhD Thesis, Imperial College London (2003).

[47] A. Ivankovic, K.C. Pandya, J.G. Williams, Eng. Fract. Mech. 71 (2004) 657-668.

[48] V. Cooper, PhD Thesis, School of Electrical, Electronic and Mechanical Engineering, University College Dublin. (2011).

[49] D. McAuliffe, A. Karac, N. Murphy, A. Ivankovic, in:, Proceedings of the 34th Annual Meeting of the Adhesion Society, Savannah, Georgia, 2011.

[50] D. McAuliffe, A. Karac, N. Murphy, A. Ivankovic, in:, Proceedings of the 11th Triennial International Conference on the Science and Technology of Adhesion and Adhesives, York, UK, 2011.

[51] D. McAuliffe, A. Karac, N. Murphy, A. Ivankovic, in:, 6th International Conference on Fracture of Polymers, Composites and Adhesives, Les Diablerets, Switzerland, 2011.

[52] OpenFOAM Foundation www.openfoam.com, (2012).

[53] V. Cooper, A. Ivankovic, A. Karac, D. McAuliffe, Z. Tukovic, N. Murphy, in:, Proceedings of the 32nd Annual Meeting of the Adhesion Society, Savannah, Georgia, 2009, pp. 33-35.

[54] A. Karac, B.R.K. Blackman, V. Cooper, A.J. Kinloch, S. Rodriguez Sanchez, W.S. Teo, A. Ivankovic, Eng. Fract. Mech. 78 (2011) 973-989.

[55] I. Georgiou, H. Hadavinia, A. Ivankovic, A.J. Kinloch, V. Tropsa, J.G. Williams, J. Adhes. 79 (2003) 239-265.

[56] V. Cooper, A. Ivankovic, A. Karac, in:, Proceedings of the 33rd Annual Meeting of the Adhesion Society, Daytona Beach, Florida, 2010.

[57] H. Hadavinia, L. Kawashita, A.J. Kinloch, D.R. Moore, J.G. Williams, Eng. Fract. Mech. 73 (2006) 2324-2335.

[58] Y.L. Liang, R.A. Pearson, Polymer 50 (2009) 4895-4905.

[59] T.H. Hsieh, A.J. Kinloch, K. Masania, A.C. Taylor, S. Sprenger, Polymer 51 (2010) 6284-6294.

[60] R.A. Pearson, L.N. Bacigalupo, Y.L. Liang, B.T. Marouf, R.K. Oldak, in:, Proceedings of the 31st Annual Meeting of The Adhesion Society, Austin, Texas, 2008.

[61] Y. Huang, A.J. Kinloch, J. Mat. Sci. 27 (1992) 2753-2762.

[62] Y. Huang, A.J. Kinloch, J. Mat. Sci. 27 (1992) 2763 - 2769.

[63] National Institute of Mental Health Research Services Branch http://rsbweb.nih.gov/ij, (2011).

[64] P. Echlin, Handbook of Sample Preparation for Scanning Electron Microscopy and X-Ray Microanalysis, Springer, 2009.

[65] F.J. Guild, A.C. Taylor, A.J. Kinloch, in:, Proceedings of the 32nd Annual Meeting of the Adhesion Society, Savannah, Georgia, 2009.